Acta Crystallographica Section D
Biological Crystallography
ISSN 0907-4449

S-SAD phasing study of death receptor 6 and its solution conformation revealed by SAXS

Heng Ru,[a,b]‡ Lixia Zhao,[a]‡ Wei Ding,[a]‡ Lianying Jiao,[a] Neil Shaw,[a,c] Wenguang Liang,[a] Liguo Zhang,[a] Li-Wei Hung,[d] Naohiro Matsugaki,[e] Soichi Wakatsuki[e] and Zhi-Jie Liu[a,c]*

[a]National Laboratory of Biomacromolecules, Institute of Biophysics, Chinese Academy of Sciences, Beijing 100101, People's Republic of China, [b]Graduate University of Chinese Academy of Sciences, Beijing 100 049, People's Republic of China, [c]Institute of Molecular and Clinical Medicine, Kunming Medical University, Kunming 650500, People's Republic of China, [d]Physics Division, Los Alamos National Laboratory, Los Alamos, NM 87545, USA, and [e]Structure Biology Research Center, Photon Factory, Institute of Materials Structure Science, High Energy Accelerator Research Organization (KEK), Oho 1-1, Tsukuba, Ibaraki 305-0801, Japan

‡ These authors contributed equally to this work.

Correspondence e-mail: zjliu@ibp.ac.cn

Received 20 January 2012
Accepted 2 February 2012

PDB References: death receptor 6, data set *A*1, 3u3p; data set *A*2, 3u3q; data set *B*1, 3u3s; data set *C*1, 3u3v; data set *D*1, 3u3t.

A subset of tumour necrosis factor receptor (TNFR) superfamily members contain death domains in their cytoplasmic tails. Death receptor 6 (DR6) is one such member and can trigger apoptosis upon the binding of a ligand by its cysteine-rich domains (CRDs). The crystal structure of the ectodomain (amino acids 1–348) of human death receptor 6 (DR6) encompassing the CRD region was phased using the anomalous signal from S atoms. In order to explore the feasibility of S-SAD phasing at longer wavelengths (beyond 2.5 Å), a comparative study was performed on data collected at wavelengths of 2.0 and 2.7 Å. In spite of sub-optimal experimental conditions, the 2.7 Å wavelength used for data collection showed potential for S-SAD phasing. The results showed that the $R_{\rm ano}/R_{\rm p.i.m.}$ ratio is a good indicator for monitoring the anomalous data quality when the anomalous signal is relatively strong, while $d''/{\rm sig}(d'')$ calculated by *SHELXC* is a more sensitive and stable indicator applicable for grading a wider range of anomalous data qualities. The use of the 'parameter-space screening method' for S-SAD phasing resulted in solutions for data sets that failed during manual attempts. SAXS measurements on the ectodomain suggested that a dimer defines the minimal physical unit of an unliganded DR6 molecule in solution.

1. Introduction

The tumour necrosis factor (TNF) superfamily consists of ligands and receptors that play pivotal roles in regulating immune responses during normal and disease states (Aggarwal, 2003). For example, TNF-α is a monocyte-derived cytotoxin that plays a role in pro-inflammation, host defence against cellular microbial infections and tumour regression (Körner & Sedgwick, 1996). TNF-β (also called lymphotoxin α; LT-α), which is produced by lymphocytes, mediates inflammatory, immunostimulatory and antiviral responses as well as the formation of secondary lymphoid organs during development (Körner & Sedgwick, 1996). Natural killer cells express CD95L ligands, which induce caspase-mediated apoptosis upon an encounter with infected cells (Nagata & Golstein, 1995). More than 20 such ligands that are involved in modulating or orchestrating immune responses and belong to the TNF superfamily have been identified. These ligands exert their function by binding highly modular receptors containing three well defined regions: cysteine-rich domains exposed on the surface of the cells, a transmembrane region and a cytoplasmic effector region that relays the message to the adaptor protein, culminating in an elaborate response which could result in either apoptosis, proliferation, survival or differentiation (Aggarwal, 2003). For instance, TNF-α and TNF-β relay signals through two surface receptor molecules TNFR I

(p55) and TNFR II (p75). The binding sites for the receptor on the trimeric ligands are located at the interface between the ligand molecules, and signalling is triggered by the oligomerization of the cytoplasmic domain of the receptor molecule upon ligand binding (Banner *et al.*, 1993; Mukai *et al.*, 2010). However, unliganded TNFR I molecules can self-associate into dimers of two different types. The first type, observed at neutral pH, is comprised of parallel dimers in which the dimer interface is well separated from the TNF-binding site and the binding of ligand leads to clustering of the receptor. The second type, also observed at neutral pH, forms antiparallel dimers in which the ligand-binding site is overlapped in order to avoid triggering signalling in the absence of TNF (Naismith *et al.*, 1995). Furthermore, at low-pH conditions TNFR I can also form antiparallel dimers that occlude the TNF-binding site, and the formation of such dimers mimics the disassociation of the receptor–ligand complex within the endosome (Naismith *et al.*, 1996). The members of the TNF receptor superfamily can be classified into three groups based on the type of signalling domain present in the cytoplasmic tail of the receptor. One group of receptors, called the death receptors (DRs), are characterized by the presence of one or more death domains in their cytoplasmic tails (Itoh & Nagata, 1993; Tartaglia *et al.*, 1993). The second group of receptors transmit messages *via* TNF receptor-associated-factor-interacting motifs (TIMs) found in their cytoplasmic tails (Arch *et al.*, 1998). Interestingly, the third group of receptors do not contain any signalling motifs but are suggested to regulate the immune response by acting as decoys and competing with other receptors for ligands (Ashkenazi, 2002).

To date, six types of death receptors are known, which upon binding a ligand recruit either the Fas-associated death domain (FADD) or the TNF-receptor-associated death domain (TRADD) adaptor proteins. Recruitment of FADD results in the assembly of death-inducing signalling complex (DISC), culminating in apoptosis (Wilson *et al.*, 2009). In contrast, recruitment of the adaptor TRADD results in the formation of a complex in the plasma membrane capable of activating the NK-κB, JNK and p38 MAP kinase pathways, which could stimulate either proliferation, differentiation or apoptosis. Although the death receptors share similar topologies, they bind distinct ligands. The low sequence identity observed between the receptors seems to confer the ligand specificity. Except for DR6, ligands for all of the death receptors are known. Recently, DR6 has been shown to participate in neural pruning by recruiting caspases. Specifically, DR6 was shown to bind an N-terminal (1–286) fragment of amyloid precursor protein (APP) generated after its cleavage from the surface by β-secretase, resulting in caspase-dependent degeneration of neurons (Nikolaev *et al.*, 2009). However, in a related study Klíma and coworkers showed that N-APP and its homologue amyloid precursor-like protein-2 (N-APLP2) produced using HEK293FT cells or in *Escherichia coli* could not bind DR6 or activate the transcription factor NK-κB and stress kinases from the JNK/SAPK family (Klíma *et al.*, 2011). Moreover, a recent study on DR6 concluded that regulation of oligodendrocyte survival and maturation as well as myelination is carried out through a mechanism independent of N-APP (Mi *et al.*, 2011). Thus, the nature of the ligand for DR6 is not clearly understood.

The goal of this study was to obtain a structural view of DR6 using X-ray crystallography and to characterize its oligomeric state in solution using small-angle X-ray scattering (SAXS). The ectodomain of all of the death receptors is rich in cysteines. Therefore, the anomalous signal of sulfur can be used as a probe for solving the phase problem during structure determination. The single-wavelength anomalous scattering of S atoms (S-SAD) is an emerging phasing technique for routine crystal structure determination. Compared with the anomalous signals from conventional heavy atoms such as Se, Pt, Hg or Au in the commonly used wavelength ranges of most X-ray sources for macromolecular crystallography, the strength of the anomalous signal of sulfur is relatively weak. This disadvantage has not prevented researchers from using S-SAD for *de novo* crystal structure determinations. The concept of using the anomalous signal of sulfur to assist in structure determination was explored experimentally by Hendrickson & Teeter (1981) and theoretically by Wang (1985). The first successful use of S-SAD for protein structure determination was reported for crambin (Hendrickson & Teeter, 1981); the structure of this 4.72 kDa protein was phased by the resolved anomalous scattering (RAS) method (Hendrickson & Teeter, 1981). The RAS method used to determine the crambin structure requires a large contribution of $\sim$1.4% of the total scattering power of the sulfur substructure to the Bijvoet differences, which is much greater than that observed for most proteins. Because of this limitation, no new structures were determined using the S-SAD method for many years until a test study on lysozyme (Dauter *et al.*, 1999) and the *de novo* crystal structure determination of obelin using long-wavelength synchrotron X-rays (Liu *et al.*, 2000). Two important factors contributed to the success of the lysozyme and obelin cases: (i) the development of the iterative single-wavelength anomalous scattering (ISAS) method coupled with solvent flattening (Wang, 1985) and (ii) advances in instrumentation and data-processing software which ensured the collection and processing of much more accurate anomalous diffraction data. Since then, many more *de novo* crystal structures have been solved using synchrotron X-rays (Gordon *et al.*, 2001; Ramagopal *et al.*, 2003; Brown *et al.*, 2002; Weiss *et al.*, 2004; Li *et al.*, 2002; Madauss *et al.*, 2004; Agarwal *et al.*, 2006; Wagner *et al.*, 2006; Lakomek *et al.*, 2009; Goulet *et al.*, 2010) or in-house Cu or Cr X-rays (Yang & Pflugrath, 2001; Debreczeni, Bunkóczi, Girmann *et al.*, 2003; Debreczeni, Bunkóczi, Ma *et al.*, 2003; Yang *et al.*, 2003; Kitago *et al.*, 2005; Nagem *et al.*, 2005; Watanabe *et al.*, 2005; Ren *et al.*, 2005; Sarma & Karplus, 2006; Nan *et al.*, 2009; Li *et al.*, 2008).

Owing to the poor strength of anomalous signal in S-SAD experiments, success in recording the anomalous signal of sulfur is largely dependent on experimental conditions, such as the diffraction quality of the crystal, the instrumentation and the data-collection strategy. For a specific crystal and data-collection system, the strategy employed for data collection is often the only key factor that has an impact on data quality. Among the variables associated with data-collection strategies

involving longer wavelengths (Cianci *et al.*, 2008; Ramagopal *et al.*, 2003), the choice of the wavelength is one of the most important factors. To date, wavelengths for successful cases of *de novo* S-SAD phasing have mostly been within the range 1.54–2.50 Å (Lakomek *et al.*, 2009; Weiss *et al.*, 2001). The relationship between S-SAD signal and data quality using X-rays of wavelength beyond 2.5 Å has rarely been studied. The optimal wavelength for an S-SAD data-collection experiment is related to characteristics of the target crystal (such as diffraction quality, sensitivity to radiation damage, size, shape, mosaicity and space group) and the instrumentation setup (Cianci *et al.*, 2008). Because of the general applicability of S-SAD methods, several synchrotron beamlines have already been dedicated to data collection at longer wavelengths for phasing purposes, while new ones are being built. A comparative study of the quality of diffraction data collected at X-ray wavelengths longer and shorter than 2.5 Å would help to validate the advantages of collecting S-SAD data using longer-wavelength X-rays. We took this approach for DR6 crystals on beamlines 17A and 1A at the Photon Factory, KEK, Japan. The latter is a designated long-wavelength beamline designed to generate 3.0 Å wavelength X-rays (not officially commissioned when our experiments were performed). Data for crystals of DR6 were collected using both 2.0 and 2.7 Å wavelength synchrotron X-rays. A series of indicators that measure the strength of anomalous signal in the diffraction data, such as the $R_{\rm ano}/R_{\rm p.i.m.}$ ratio, $d''/{\rm sig}(d'')$ and CC(all/weak), were investigated for their reliabilities and sensitivities. In addition, owing to the weak anomalous signal of sulfur, S-SAD phasing is more challenging for both crystallographers and the phasing software. There are many parameters for each program, the values of which need to be decided by users. The choice of the values of these parameters is often critical for successful structure solution using S-SAD. A 'parameter-space screening' method has been developed and coupled with a high-throughput (HT) structure-determination pipeline to overcome this problem (Liu *et al.*, 2005). Instead of choosing the values of the parameters manually based on experience, critical parameters such as the resolution for heavy-atom searching and phasing are screened in parallel in multidimensional space using a computer cluster. In this study, the 'parameter-space screening' method was demonstrated to be a powerful tool in pushing the envelope of S-SAD phasing. Two suboptimal quality anomalous data sets which failed to yield correct structure solutions by manual S-SAD phasing were successfully salvaged by the HT structure-determination pipeline.

Further, small-angle X-ray scattering (SAXS) experiments were performed in order to study the solution status of DR6. The SAXS measurements on the ectodomain suggested that a dimer defines the minimal physical unit of an unliganded DR6 molecule in solution. Two molecules of the protein could be fitted into the low-resolution envelope of unliganded DR6 generated by SAXS.

Here, we report and discuss (i) the feasibility of using S-SAD data collection at longer wavelengths, (ii) the utility of more general indicators for accessing the quality of anomalous diffraction data, (iii) the 'parameter-space screening'-based S-SAD phasing pipeline and (iv) the solution-status analysis of DR6 by small-angle X-ray scattering (SAXS).

2. Materials and methods

2.1. Cloning, expression and purification

The cDNA encoding the ectodomain of human death receptor 6 (amino acids 1–348) as well as cysteine-rich domains (CRDs) 1–4 only (amino acids 1–214) and a C-terminal 6×His tag were subcloned in frame into the vector pFastbac1 (Invitrogen) by *Bam*HI and *Xho*I restriction sites and confirmed by sequencing. The plasmids containing the gene of interest were then transformed into DH10Bac competent cells (Invitrogen) and the recombinant bacmid DNA was isolated and verified according to the Bac-to-Bac Baculovirus Expression System (Invitrogen) instructions. Sf9 insect cells were then transfected to generate recombinant baculovirus and the titre of baculoviral stock was amplified by infecting the Sf9 insect cells with P1 and P2 viral stocks.

The ectodomain and CRDs 1–4 of the recombinant human death receptor 6 with a C-terminal 6×His tag were expressed as secreted protein by infecting Sf9 insect cells with recombinant baculovirus at an optimal MOI. The culture medium containing the secreted recombinant protein was harvested after 72 h infection.

For expression of the ectodomain of recombinant human death receptor 6 in mammalian cells, the cDNA was subcloned in frame into the vector pTT3 by *Eco*RI and *Bam*HI restriction sites with a C-terminal 6×His tag and further confirmed by sequencing. The plasmid was transiently transfected into HEK293 cells and the culture medium containing the secreted target protein was collected and supplemented for 6 d.

For purification, the culture medium containing the target protein either from the insect cells or the mammalian cells was first centrifuged at 12 000 rev min^{-1} at 277 K for 1 h to remove the cells and cell debris and was then loaded onto HiTrap Ni Fast Flow beads (GE Healthcare) previously equilibrated with 50 m*M* phosphate-buffered saline (PBS; 50 m*M* Na_2HPO_4, 10 m*M* KH_2PO_4, 137 m*M* NaCl, 2.7 m*M* KCl pH 7.4) at 277 K. The remaining steps were similar to those described previously by Su *et al.* (2010). In brief, the beads were washed on a gravity column using 50 m*M* PBS with 20 m*M* imidazole pH 7.4 and eluted with 50 m*M* PBS supplemented with 300 m*M* imidazole pH 7.4. The protein was then applied onto a HiTrap heparin column, eluted with a 150–1000 m*M* NaCl gradient and further purified on a gel-filtration column equilibrated with 20 m*M* Tris–HCl 150 m*M* NaCl, 1 m*M* DTT pH 7.5. The pooled peak fractions were concentrated to 20 mg ml^{-1} and aliquots were flash-cryocooled into liquid nitrogen and stored at 193 K until further use. The yield of recombinant protein was about 7 mg per litre of culture.

2.2. Crystallization

The full-length ectodomain (amino acids 1–348) of DR6 produced by insect cells and treated with PNGase F was set

Table 1
Data-collection and refinement statistics.

Values in parentheses are for the highest resolution shell.

Crystal	*A*	*A*	*B*	*C*	*D*
Data set	*A*1	*A*2	*B*1	*C*1	*D*1
PDB code	3u3p	3u3q	3u3s	3u3v	3u3t
X-ray source	17A	17A	17A	1A	1A
Crystal-to-detector distance (mm)	310	160	160	91	91
No. of images	360	360	360	248	281
Oscillation width (°)	0.5	1	1	1	0.75
Wavelength (Å)	0.98	2.00	2.00	2.70	2.70
Space group	$P6_122$	$P6_122$	$P6_122$	$P6_122$	$P6_122$
Unit-cell parameters (Å)					
a	77.86	77.91	77.68	77.56	77.47
c	186.56	186.42	186.81	187.41	185.81
Mosaicity (°)	0.32	0.48	0.22	0.38	0.65
No. of molecules in asymmetric unit	1	1	1	1	1
Resolution range (Å)	50.00–2.09 (2.16–2.09)	50.00–2.70 (2.82–2.70)	50.00–2.70 (2.82–2.70)	50.00–2.95 (3.08–2.95)	50.00–3.20 (3.34–3.20)
R_{merge} (%)	6.4 (25.5)	7.5 (37.3)	9.7 (38.0)	11.4 (42.4)	10.4 (36.4)
Mean $I/\sigma(I)$	79.09 (15.79)	80.782 (21.0)	73.15 (14.9)	60.70 (12.76)	54.10 (12.47)
Completeness (%)	99.9 (100.0)	99.9 (99.9)	99.9 (99.7)	99.8 (99.8)	99.8 (99.9)
Multiplicity	20.4	39.1	39.3	25.3	20.1
Refinement					
Resolution (Å)	38.11–2.09	50.00–2.70	50.00–2.70	50.00–2.96	50.00–3.21
No. of reflections	19478	9338	9308	7227	5655
R_{work}/R_{free} (%)	22.53/27.05	19.51/23.54	19.65/26.01	19.24/25.70	20.79/26.08
No. of atoms	1375	1375	1375	1375	1233
No. of protein atoms	1233	1233	1233	1233	1233
No. of waters	142	142	142	142	0
Wilson *B* (Å^2)	30.1	65.9	62.4	89.7	102.9
Mean *B* (Å^2)	35.3	44.3	41.0	51.0	57.4
R.m.s. deviations					
Bond lengths (Å)	0.023	0.020	0.017	0.017	0.015
Bond angles (°)	2.4	2.1	2.0	2.0	1.9
Ramachandran analysis (%)					
Favoured region	93.2	93.2	93.8	91.9	91.3
Allowed region	4.97	3.73	3.73	6.83	5.59
Outliers	1.86	3.10	2.48	1.24	3.11

up for crystallization immediately after purification. Crystallization screening was carried out by the sitting-drop vapour-diffusion method using commercial screening kits from Hampton Research and Emerald BioSystems. 0.4 µl protein stock solution was mixed with 0.4 µl reservoir using a Mosquito robot (TTP LabTech) and equilibrated against 40 µl reservoir at 289 K. Initial hits were further optimized by the hanging-drop vapour-diffusion method by mixing 1 µl protein solution (10 mg ml^{-1}) and 1 µl reservoir solution at 289 K. Diffraction-quality crystals were obtained in at least two conditions: (i) 0.2 *M* ammonium acetate, 0.1 *M* sodium citrate tribasic dehydrate pH 5.0–6.0, 25–30% PEG 4000 and (ii) 0.1 *M* HEPES pH 7.0–7.5, 1.5–1.7 *M* ammonium sulfate, 2% PEG 400. The crystals used in this study were obtained from these conditions.

2.3. Data collection, phasing, structure solution and refinement

2.3.1. Data collection and data processing. Crystals were cryocooled in liquid nitrogen prior to diffraction testing and data collection. Four DR6 crystals, denoted *A*, *B*, *C* and *D* in the subsequent descriptions, were used for data collection. Crystal *A* was first used to collect data on beamline 17A with 0.98 Å wavelength X-rays for higher resolution refinement. A total of 360 0.5° oscillation images were collected. Subsequently, crystals *A* and *B* were used to collect data with 2.00 Å wavelength X-rays on beamline 17A, while crystals *C* and *D* were used to collect data on beamline 1A with 2.70 Å wavelength X-rays. Crystals *A* and *B* were cooled with nitrogen gas at 100 K on beamline 17A, while crystals *C* and *D* were cooled with helium gas at 100 K on beamline 1A during data collection. To reduce the scattering of the long-wavelength X-rays, the detector on beamline 1A was enclosed in a box filled with helium gas. All diffraction images were indexed and scaled using *HKL*-2000 (Otwinowski & Minor, 1997). Data-collection and data-processing parameters are given in Table 1.

2.3.2. Phasing, model building and refinement. All of the scaled long-wavelength data were subjected to the following steps for phasing and quality assessment. The high-throughput (HT) crystal structure-determination pipeline X^{2}DF (Liu *et al.*, 2005) was used for heavy-atom substructure determination, S-SAD phasing, density modification and automated model building based on the 'parameter-space screening' method (Liu *et al.*, 2005). In the current version of the X^{2}DF pipeline, users have the option to choose either a *SOLVE–RESOLVE–DM–DMMULTI–ARP*/*wARP* pipeline or a *SHELXC*/*D–SHELXE–DM–DMMULTI–ARP*/*wARP* pipeline. In this specific case, the pipeline was composed of *SHELXC*/*D* for heavy-atom substructure determination, *SHELXE* for phasing (Sheldrick, 2008), *DM* and *DMMULTI* (Cowtan, 1994) for phase extension and multi-crystal averaging with high-resolution data set *A*1, and *ARP*/*wARP* (Langer *et al.*, 2008) for model building. Two-dimensional parameter-space screening was performed. The two screening parameters applied were high-resolution limits for heavy-atom searching and phasing (screening resolution range, 4.0 Å to high-resolution end for each data set; step, 0.2 Å). The parameter-space screening results are listed in Table 2. The model built by *flex-wARP* was subjected to several cycles of manual model fitting and rebuilding using *Coot* (Emsley *et al.*, 2010) and refinement using *REFMAC* (Murshudov *et al.*, 2011) and *phenix.refine* (Adams *et al.*, 2010) alternately. Details of data-collection and refinement statistics are listed in Table 1. The quality of the final model was validated with *MolProbity* (Chen *et al.*, 2010).

Table 2
Phasing and anomalous signal analysis of data collected at different wavelengths.

Data set	*A*2	*B*1	*C*1	*D*1
Wavelength (Å)	2.00	2.00	2.70	2.70
Data resolution (Å)	50.00–2.70	50.00–2.70	50.00–2.95	50.00–3.20
Best heavy-atom searching resolution (Å)	4.00	3.80	3.60	N/A
Best phasing resolution (Å)	3.50	2.50	3.30	N/A
χ† (%)	2.14		3.61	
$R_{\rm anom}$‡	0.023	0.033	0.054	0.059
$R_{\rm p.i.m.}$§	0.015	0.033	0.049	0.051
$R_{\rm anom}/R_{\rm p.i.m}$	1.53	1.00	1.10	1.16
$d''/{\rm sig}(d'')$¶	1.80	1.32	1.15	0.88
CC(all/weak)††	47.40/23.42	30.16/9.55	35.79/11.22	34.19/10.83
$\Delta\varphi$‡‡	66.56	69.73	70.90	74.04

† $\chi = \langle\Delta F_{\rm anom}\rangle/\langle F_{\rm P}\rangle = (2N_{\rm A}/N_{\rm P})^{1/2} \times (\Delta f_{\rm A}''/Z_{\rm eff})$, where $N_{\rm A}$ is the number of anomalous scatterers, $N_{\rm P}$ is the approximate total number of non-H atoms and $Z_{\rm eff}$ is the effective atomic number (~6.7 for non-H protein atoms). ‡ $R_{\rm anom} = 100\sum_{hkl}|I(hkl) - I(\overline{hkl})|/\sum_{hkl}\langle I(hkl)\rangle$. § $R_{\rm p.i.m.} = 100\sum_{hkl}\{1/[N(hkl)-1]\}^{1/2}\sum_i|I_i(hkl) - \langle I(hkl)\rangle|/\sum_{hkl}\sum_i I_i(hkl)$. ¶ Calculated in the 50.00–3.10 Å resolution range. †† Correlation coefficient in *SHELXD*. ‡‡ Average phase difference between model phases and S-SAD experimental phases calculated by the program *CPHASEMATCH* in the *CCP*4 suite.

2.3.3. Anomalous data analysis and comparison. The long-wavelength data quality in terms of the anomalous signal of sulfur was evaluated based on the following parameters.

(i) $R_{\rm ano}/R_{\rm p.i.m.}$: $R_{\rm ano}$ was calculated by *SHELXC* (Sheldrick, 2008). In order to obtain $R_{\rm p.i.m.}$, the raw images were reprocessed with *MOSFLM* (Battye *et al.*, 2011; Leslie, 2006) and scaled with *SCALA* (Evans, 2006) in the *CCP*4 suite.

(ii) $d''/{\rm sig}(d'')$: as computed by *SHELXC* (Sheldrick, 2008) between 50.00 and 3.10 Å resolution.

(iii) CC (all/weak): correlation coefficient of all/weak data calculated by *SHELXD* (Sheldrick, 2008).

(iv) $\Delta\varphi$: average phase difference between model phases and experimental S-SAD phases calculated by *CPHASEMATCH* (Winn *et al.*, 2011).

The model phases were computed from the refined coordinates of each data set using the *FFT* program, while the S-SAD phases were calculated by *Phaser* (McCoy *et al.*, 2007), where the sulfur sites were extracted from the refined coordinates. The results are listed in Table 2.

2.4. SAXS data collection and analysis

Initial SAXS data were collected on the SIBYLS beamline at the Advanced Light Source (ALS), Lawrence Berkeley National Laboratory. All data sets were measured with three exposures, 0.5, 1 and 6 s, at 283 K. Three different concentrations of the protein, 2.5, 5 and 10 mg ml^{-1}, were used for the measurements. Data for buffers were collected between every two protein samples. The scattering data were then scaled and the average values for the buffers before and after the sample measurements were subtracted. Multiple curves with different concentrations and different exposure times were scaled and merged to generate an ideal average scattering curve. The quality of the scattering curves were analysed using the program *PRIMUS* (Konarev *et al.*, 2003) to ensure that there was no obvious aggregation and radiation damage before further analysis. The initial $R_{\rm g}$ values were calculated from the Guinier plot; only data from low q values were used for the calculation. The $P(r)$ distribution function was calculated with the program *GNOM* (Svergun, 1992). The molecular weight was estimated directly from the SAXS MoW server (http://www.if.sc.usp.br/~saxs/saxsmow.html) using the $P(r)$ distribution function (Fischer *et al.*, 2010). The low-resolution global shape of the protein in solution was modelled by the program *GASBOR* (Svergun *et al.*, 2001) using both the original scattering curve and the calculated $P(r)$ distribution curve. A total of 354 residues (including the hexa-His tag) in the asymmetric unit and *P*2 symmetry were applied in the *GASBOR* calculations. Several individual calculations were performed and they all showed that the shape of the DR6 molecules in solution was an elongated open form. Subsequently, continuous and meaningful shapes were picked up and averaged by the program *DAMAVER* (Volkov & Svergun, 2003). Two individual monomer models were superimposed onto the low-resolution model using the program *SUPCOMB* (Kozin & Svergun, 2001) to model the elongated DR6 dimer in solution.

3. Results

3.1. Sulfur SAD phasing at long wavelengths with the X^{2}DF pipeline

DR6 is highly modular, with an N-terminal ectodomain (amino acids 1–348) comprising a predicted signal peptide (amino acids 1–41), four cysteine-rich domains (amino acids 50–211), a short transmembrane region (amino acids 351–370) followed by a C-terminal death domain (amino acids 415–498) and a predicted CARD-like domain (amino acids 564–655) (Fig. 1*a*). The disulfide connectivity between the cysteine residues is crucial for DR6 to fold and to achieve the correct topology for the recognition of ligands (Fig. 1*b*). The entire ectodomain of DR6 was produced as a secreted protein and purified to homogeneity from Sf9 cells. The protein was treated with PNGase F to remove glycosylation (Fig. 1*c*). The protein crystallized in space group $P6_122$, with unit-cell parameters $a = b = 77.86$, $c = 186.56$ Å and one molecule in the asymmetric unit. Four DR6 crystals designated *A*, *B*, *C* and *D* were used for data collection at different wavelengths (shown in parentheses). Crystals *A*, *B*, *C* and *D* diffracted to 2.09 Å ($\lambda = 0.98$ Å), 2.70 Å ($\lambda = 2.0$ Å), 2.95 Å ($\lambda = 2.7$ Å) and 3.20 Å ($\lambda = 2.7$ Å) resolution, respectively (Table 1). S-SAD phasing was attempted manually with each long-wavelength data set using either *PHENIX* or *SHELXC*/*D*/*E*. Only data set *A*2 yielded the correct solution. Density-modification methods such as *DM* (Cowtan, 1994) and *B*-factor sharpening (Pannu *et al.*, 1998; Su *et al.*, 2010) were attempted for the remaining data sets, but failed to yield structure solutions. The HT structure-determination pipeline X^{2}DF was then used for phasing and automated model building, as described in §2. Surprisingly, in addition to data set *A*2, correct structural solutions were also obtained from data sets *B*1 and C1. This success could be attributed to the powerful parameter-space screening capability of the pipeline. The combinations of the best high-

resolution limits for heavy-atom search and the best resolution for phasing which led to the correct solution are shown in Table 2. From the screening results, we observed that the best high-resolution limits for heavy-atom search and phasing, 4.0 and 3.5 Å for *A*2, 3.8 and 2.5 Å for *B*1, and 3.6 and 3.3 Å for *C*1, respectively, are not within the range that crystallographers usually pick. As shown in Fig. 2(*a*), the parameter-screening space is not linear. Therefore, if the initial resolution values for heavy-atom search and phasing are in the wrong area of parameter space the calculation will not lead to a correct structure solution. Only data set *D*1 collected at 2.7 Å wavelength failed to produce the correct structure solution, presumably owing to its weak diffraction. The final model consisted of 1229 protein atoms and 183 water molecules, with an *R* value of 20.53% and an $R_{\rm free}$ value of 24.12% (Table 1). Electron density for residues 51–214 was clearly defined, allowing the unambiguous placement of side chains (Fig. 2*b*). However, residues 1–50 and 215–348 could not be traced owing to a lack of clear electron density. The protein seems to have degraded during the course of crystallization. SDS–PAGE analysis of protein recovered from a crystal of DR6 ectodomain revealed a lower molecular-weight band matching the molecular weight of residues 51–214 observed in the crystal structure.

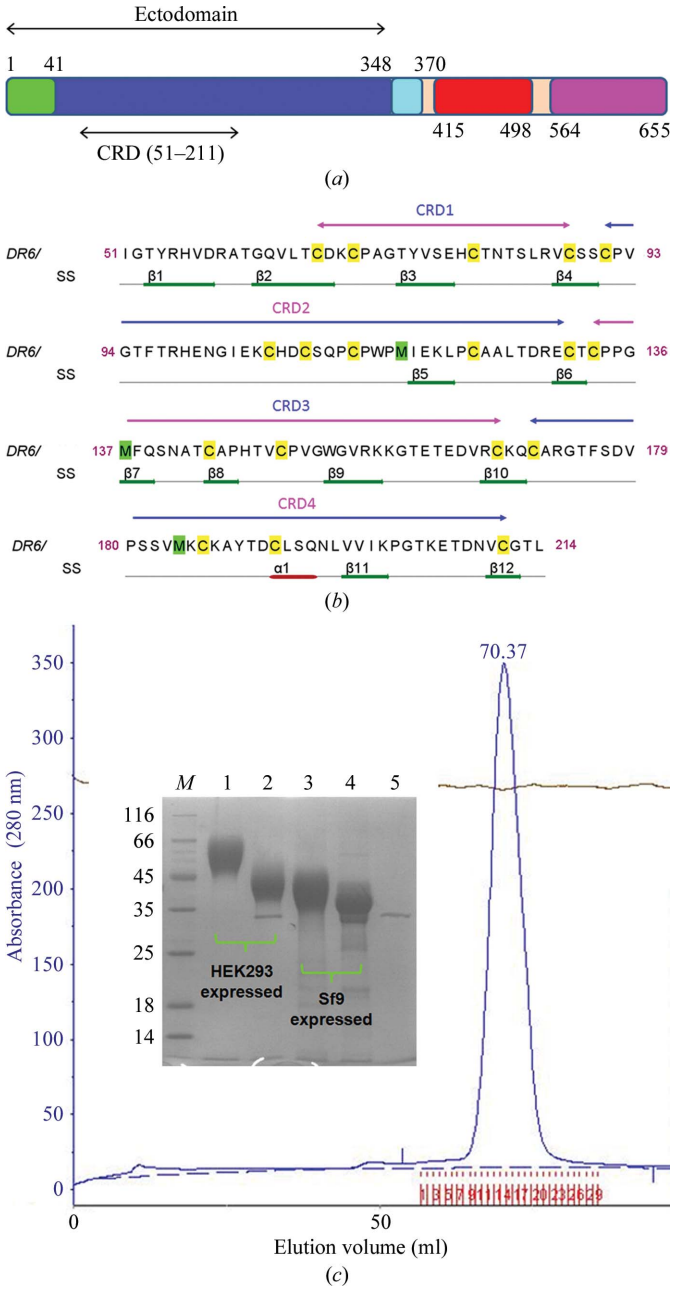

Figure 1
Domain organization of DR6. (*a*) A diagrammatic representation of DR6 showing the domain boundaries. The transmembrane region (cyan), death domain (red) and CARD domain (magenta) were not part of the clone used for structural studies. (*b*) Sequence of the CRD domain showing the locations of the S atoms used for phasing. (*c*) Size-exclusion profile of deglycosylated DR6 ectodomain. The protein was expressed using Sf9 cells. The SDS–PAGE gel picture (inset) shows the PNGase F-treated protein (lanes 2 and 4) migrating faster than the untreated control (glycosylated DR6; lanes 1 and 3). Lane *M* contains molecular-weight markers (labelled in kDa). Lane 5 contains PNGase F.

3.2. Comparison of data collected at wavelengths of 2.0 *versus* 2.7 Å

Residues 51–214 of the DR6 molecule contain 21 S atoms from 18 cysteines and three methionines (Fig. 1*b*). There are nine disulfide bonds spread across the length of the protein (Fig. 2*c*). The estimated Bijvoet amplitude ratio χ was calculated using the equation $\chi = \langle\Delta F_{\rm anom}\rangle/\langle F_{\rm P}\rangle = (2N_{\rm A}/N_{\rm P})^{1/2} \times (\Delta f''_{\rm A}/Z_{\rm eff})$, where $N_{\rm A}$ and $N_{\rm P}$ are the number of anomalous scatters and the approximate total number of non-H atoms, respectively, and $Z_{\rm eff}$ is the effective atomic number (~6.7 for non-H protein atoms; Hendrickson & Teeter, 1981). The calculated χ values for DR6 crystals are 2.14 and 3.61% for 2.0 and 2.7 Å X-rays, respectively. A longer wavelength seems to offer a larger Bijvoet intensity ratio and is therefore more likely to be the wavelength of choice for S-SAD data collection for DR6. In addition to the Bijvoet intensity ratio, we calculated the $R_{\rm ano}/R_{\rm p.i.m.}$ ratio, $d''/{\rm sig}(d'')$, CC(all/weak) and $\Delta\varphi$ for all of the data sets to compare data qualities and to identify the most informative parameters as quality indicators (Table 2). The results showed that the $R_{\rm ano}/R_{\rm p.i.m.}$ ratios for crystals *A*, *B*, *C* and *D* were 1.53, 1.00, 1.10 and 1.16, respectively. Weiss and coworkers have suggested that an $R_{\rm ano}/R_{\rm p.i.m.}$ ratio of 1.5 or greater is more likely to produce successful structure solution (Weiss *et al.*, 2001, 2004). Our results support this conclusion and we were able to solve the structure for the data set collected using crystal *A* either manually or using the pipeline without any problem. However, the $R_{\rm ano}/R_{\rm p.i.m.}$ ratio could not distinguish the quality of data sets *B*1, *C*1 and *D*1, and in fact the worst data set *D*1 actually gave a higher score (1.16) than those of data sets *B*1 (1.00) and *C*1 (1.10). In fact, data set *A*2 also gave the highest score using other indicators such as $d''/{\rm sig}(d'')$ (1.80), CC(all/weak) (47.40/23.42) and $\Delta\varphi$ (66.56), indicating its superior data quality benefitted by the better diffraction capability of crystal *A* compared with the other three crystals. Furthermore, the $d''/{\rm sig}(d'')$ values for data sets *B*1, *C*1 and *D*1 agreed well with the phasing results and $\Delta\varphi$ values, as shown in Table 2,

suggesting that $d''/\mathrm{sig}(d'')$ values are better suited for accessing suboptimal quality anomalous data sets.

3.3. Overall structure

The ectodomain of DR6 folds into a long elongated structure with a bend at the centre. The structure resembles a V-shaped boomerang (Fig. 2*c*). Each wing of the boomerang-shaped structure is made up of a pair of CRDs. Within each pair, each CRD is twisted with respect to the other along the long axis. The integrity of the elongated structure is maintained by disulfide bonds that are observed to punctuate the structure at regular intervals along the long axis (Fig. 2*c*).

Although the members of the TNFR family of receptors share very low sequence identity, their overall structure is similar. Thus, specificity is achieved using the variable primary sequence while keeping the fold conserved. CRDs are usually made up of two components: A and B motifs. These motifs can be further divided into different types based on the sequence, number and type of disulfide linkages (Naismith & Sprang, 1998). Occasionally, partial CRDs containing only one of the motifs are observed. For example, CRD1 of DR6 has only one B2 motif, made up of antiparallel β-strands stabilized by two disulfide bonds. In contrast, CRD2 of DR6 has both A1 and B2 modules. The A1 module consists of a long C-shaped loop typical of similar modules found in other CRDs. The A1 module is stabilized by a single disulfide bond and is observed to interact with the B2 module *via* several hydrogen bonds. CRD3 and CRD4 of DR6 are each made up of A1 and B1 modules. The modules are connected to each other within a CRD and interact with neighbouring modules from adjacent CRDs, thus simultaneously providing stable structural connectivity together with rigid topologies for interaction with ligands.

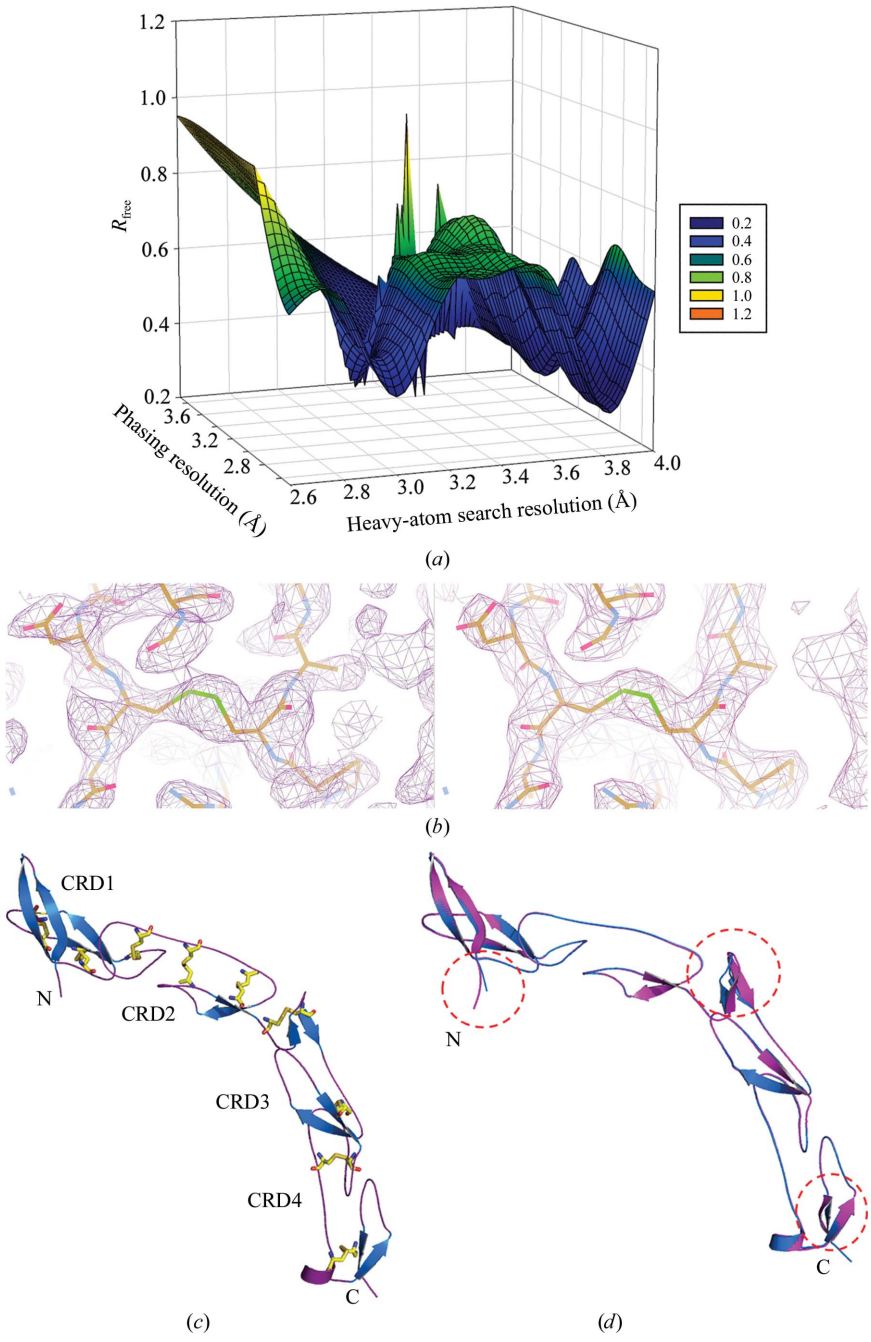

Figure 2
Structure of the CRDs of DR6. (*a*) Parameter-space screening results for data set *B*1 (2.70 Å; λ = 2.0 Å). High-resolution limits for heavy-atom search (*x* axis) and phasing (*y* axis) were screened for solutions with lowest R_{free} (*z* axis). Colours representing the respective R_{free} values are shown in a box on the right. For example, a dark blue colour represents an R_{free} value of 0.20. (*b*) Left, a section of the S-SAD-phased experimental electron-density map at a 1.0σ contour level; right, the same region after refinement. (*c*) Overall structure of the CRDs shown as a cartoon. The disulfide linkages are depicted as sticks. (*d*) Superimposition of the CRD structure (magenta; PDB entry 3qo4) on the sulfur-phased structure of this study (blue). Minor differences between the structures are circled.

While the structure–function data for the ectodomain of DR6 were being analyzed and collated, a manuscript by Kuester and coworkers describing the structure of the CRDs of DR6 was published (Kuester *et al.*, 2011). The structural boundaries of DR6 in both structures are similar, implying that this region of DR6 is rigid and compact. The region consisting of amino acids 51–214 of DR6 folds into four cysteine-rich domains, with nine disulfide bonds playing a role in shaping the contours and topology of the receptor. Except for small differences in the position of C^{α} atoms in the regions comprising amino acids 137–146, 192–198 and 210–212, the two DR6 structures are identical (Fig. 2*d*). These regions have been speculated to function as hinges to increase the plasticity of DR6 and expand the repertoire of ligands bound by DR6.

3.4. SAXS analysis of the DR6 ectodomain

Although we expressed the entire ectodomain (amino acids 1–348) for crystallization, density could only be observed for residues 51–214 of DR6. The region consisting of amino acids 51–214 was re-cloned, expressed in Sf9 cells and purified to homogeneity. Sedimentation-velocity experiments indicated that the region consisting of amino acids 51–214 of DR6 exists as a monomer in solution (data not shown). Since receptors belonging to the TNF family are known to function as dimers or trimers, the results of the sedimentation-velocity experiments on amino acids 51–214 of DR6 seemed to suggest that the interface of oligomerization resides after residue 214. To identify the oligomeric state of DR6, we conducted SAXS experiments with freshly prepared ectodomain of DR6 (residues 1–348) produced using HEK293 cells and processed in the presence of a cocktail of protease inhibitors. Different concentrations of the protein were tested in SAXS experiments (Fig. 3*a*) to exclude aggregation and radiation-damage effects. Radius of gyration (R_g) values were calculated both from Guinier plot approximation and from the indirectly Fourier transformed $P(r)$ distribution function (Fig. 3*b*). The R_g values suggested an elongated conformation with a d_{max} of 150–180 Å and the $P(r)$ distribution function estimated a molecular weight of 142 kDa for DR6 in solution. However, a monomer of the ectodomain (amino acids 1–348) has a theoretical molecular weight of only 37.5 kDa. Interestingly, the ectodomain of DR6 purified from protein expressed in HEK293 cells migrated as a 60 kDa band on SDS–PAGE. These discrepancies in the measurement of the molecular weight were expected because the ectodomain of DR6 has a long elongated shape and is glycosylated by HEK293 cells. The Kratky plot assumed an almost bell-shaped curve, in agreement with the elongated structure of the protein (Fig. 3*c*).

The envelope of the ectodomain of DR6 (amino acids 1–348) derived from SAXS analysis suggests that the protein exists as a dimer in solution (Fig. 3*d*). Indeed, two molecules of the CRD domain (amino acids 51–214) determined in this study could fit into the envelope. The shape of the envelope extends further at the C-terminus of the structures and converges. This suggests that the dimerization of DR6 could be mediated by amino acids beyond residue 214 observed in the crystal structure and therefore amino acids 51–214 of DR6 crystallized as a monomer. In solution, the monomers within the unliganded dimer of the DR6 ectodomain are arranged in a V shape, with CRD3 and CRD4 of each monomer converging such that the regions of the monomers after CRD4 meet to form the dimer interface (Fig. 3*d*). CRD1 and CRD2 of one monomer face away from the corresponding CRDs of the other monomer, with CRD1 being the farthest away from the corresponding CRD1 of the second monomer. Interestingly, the envelope seems to protrude on either side immediately after the CRD4 region of both monomers. This extra volume could be attributed to either the glycosylation reported for a similar region of DR6 produced using mammalian cells (Klíma *et al.*, 2009) or an alternative conformation of the region 215–348 of the ectodomain. The ectodomain of DR6 is immediately followed by a transmembrane region (amino acids 349–370). The SAXS data on the full-length ectodomain of DR6 seem to suggest that amino acids 215–348, especially the latter part of this region, and probably the transmembrane region might be involved in formation of the dimer interface.

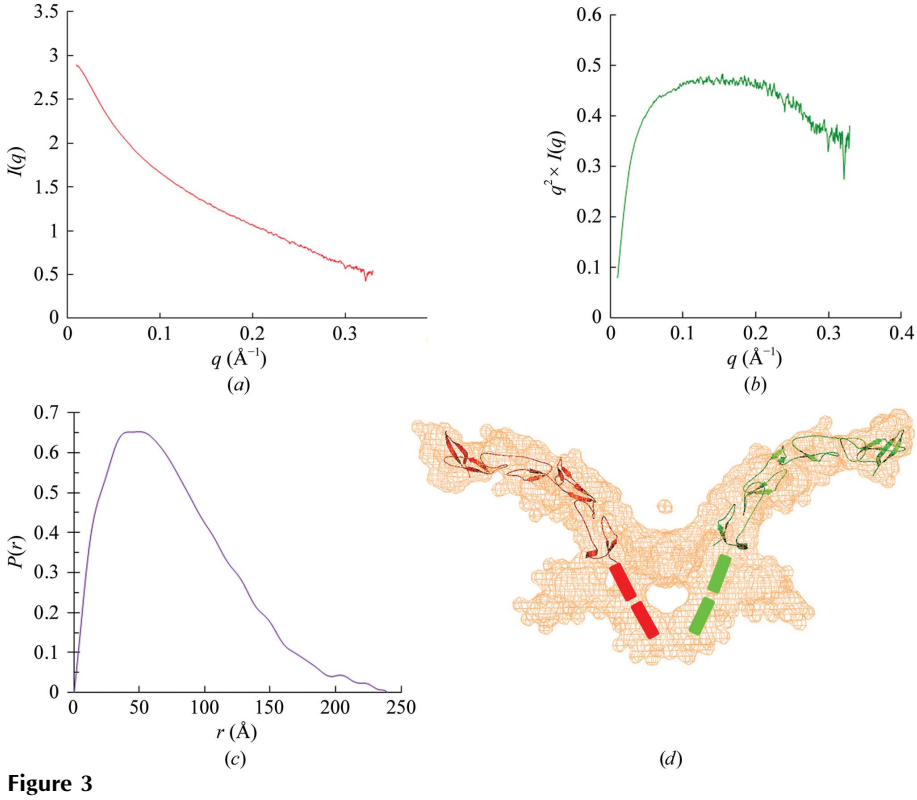

Figure 3
SAXS analysis of the ectodomain expressed in HEK293 cells. (*a*) Scattering curve and (*b*) $P(r)$ distribution function of the ectodomain of DR6. (*c*) The Kratky plot of the ectodomain assumes a bell-shaped curve, suggesting an elongated shape of the protein. (*d*) The low-resolution envelope generated from the SAXS data with two crystal structures of CRD modelled in. The region consisting of amino acids 215–348 immediately after the boundary at amino acid 214 of the crystal structure is depicted as rectangular blocks.

4. Discussion

4.1. Feasibility of data collection and S-SAD phasing using longer wavelength X-rays

The 17.9 kDa CRDs of DR6 crystallized in space group $P6_122$. The crystal structure of the DR6 CRDs was determined by S-SAD with data collected at 2.0 and 2.7 Å wavelengths using the X^{2}DF HT structure-determination pipeline. The success of S-SAD phasing depends on many factors. In this study, we tried to assess the impact of X-ray

wavelength on the sulfur anomalous signal recorded in the diffraction data and how this factor could influence the results of S-SAD phasing. A total of four crystals, *A*, *B*, *C* and *D*, were used to collect anomalous diffraction data. Data for crystals *A* and *B* were collected using 2.0 Å wavelength X-rays, while data for crystals *C* and *D* were collected using 2.7 Å wavelength X-rays.

The correct structure solution could be obtained from data collected at both wavelengths. These results suggested that although the experimental conditions for data set *C*1 were suboptimal (beamine A1 was not in the commissioning stage), the stronger anomalous signal f'' of the S atoms at 2.7 Å wavelength (1.52 e^- at 2.7 Å compared with 0.90 e^- at 2.0 Å) compensated for the difference in diffraction quality. Thus, longer wavelengths (such as 2.7 Å) offer an advantage for recording the anomalous signal from S atoms. In addition, the parameter-space screening-based HT structure-determination pipeline showed potential for S-SAD phasing by salvaging the weak anomalous data which failed to yield structure solutions by manual approaches.

It would be very useful to have reliable and sensitive indicators to judge whether a diffraction data set contains sufficient anomalous signal for phasing. Such indicators may serve as probes for a signal-based data-collection strategy where the objective of data collection is to make the anomalous signal strength indicators reach specific preset values for successful phasing. Comparison of the four long-wavelength data sets *A*2, *B*1, *C*1 and *D*1 using anomalous data-quality indicators such as the $R_{\rm ano}/R_{\rm p.i.m.}$ ratio, $d''/{\rm sig}(d'')$ and CC(all/weak) values (Table 2) clearly showed that data set *A*2 is superior to the other three data sets in terms of anomalous signal strength. The difference between the other three data sets is marginal as suggested by the phase difference $\Delta\varphi$ or the above indicators. More careful analysis revealed that the $d''/{\rm sig}(d'')$ values agree well with $\Delta\varphi$, which is considered to be a more accurate representation of the S-SAD phasing accuracy. This is corroborated by the fact that data sets *B*1 and *C*1 yielded correct structure solutions, while data set *D*1 failed to do so, in spite of all three having an $R_{\rm ano}/R_{\rm p.i.m.}$ ratio below 1.5. In general, of the three anomalous data-quality indicators, $d''/{\rm sig}(d'')$ is the most sensitive and stable probe for monitoring the strength of anomalous data.

In summary, the sulfur-phased structure of DR6 reveals an elongated ectodomain with four CRDs. Combination of the crystallographic data with the SAXS experiment results suggested a dimer of DR6 to be the biological unit in solution. We have evaluated the feasibility of employing long-wavelength X-ray beams for recording the anomalous signal of S atoms. Our results show that longer wavelengths (such as 2.7 Å) for data collection offer potential improvement of the anomalous signal of S atoms even with the trade-off of suboptimal experimental setups; the $R_{\rm ano}/R_{\rm p.i.m.}$ ratio, $d''/{\rm sig}(d'')$ and CC(all/weak) are reliable and sensitive indicators for measuring anomalous signal strength in diffraction data, while $d''/{\rm sig}(d'')$ is a more sensitive and stable indicator that is applicable for grading a wider range of anomalous data qualities. Further optimizations of the hardware and data-collection software are necessary to harness the full potential of long-wavelength X-rays for successful sulfur phasing.

The coordinates and diffraction data for data sets *A*1, *A*2, *B*1, *C*1 and *D*1 have been deposited in the Protein Data Bank with PDB codes 3u3p, 3u3q, 3u3s, 3u3v and 3u3t, respectively.

The authors thank Yun Li of the Institute of Biophysics, Chinese Academy of Sciences for help with protein expression using the insect-cell system. The authors also would like to thank the staff at beamlines 17A and 1A at the Photon Factory, KEK, Japan and beamline 12.3.1 (BL12.3.1) at the Advanced Light Source (ALS) for technical support during diffraction and SAXS data collections. BL12.3.1 is supported in part by the US Department of Energy (DOE) program Integrated Diffraction Analysis Technologies (IDAT) and the DOE program Molecular Assemblies, Genes and Genomics Integrated Efficiently (MAGGIE) under Contract No. DE-AC02-05CH11231 with the DOE. The ALS is supported by the Director, Office of Science, Office of Basic Energy Sciences of the DOE under Contract No. DE-AC02-05CH11231. This work was supported by the National Natural Science Foundation of China (grants 30870483, 31070660, 31021062 and 81072449), the Ministry of Science and Technology of China (grants 2009DFB30310, 2009CB918803 and 2011CB911103) and CAS Research Grants (YZ200839 and KSCX2-EW-J-3). This work was also supported by the NIGMS Protein Structure Initiative program (NIH U54 GM074946).

References

Adams, P. D. *et al.* (2010). *Acta Cryst.* D**66**, 213–221.
Agarwal, R., Bonanno, J. B., Burley, S. K. & Swaminathan, S. (2006). *Acta Cryst.* D**62**, 383–391.
Aggarwal, B. B. (2003). *Nature Rev. Immunol.* **3**, 745–756.
Arch, R. H., Gedrich, R. W. & Thompson, C. B. (1998). *Genes Dev.* **12**, 2821–2830.
Ashkenazi, A. (2002). *Nature Rev. Cancer*, **2**, 420–430.
Banner, D. W., D'Arcy, A., Janes, W., Gentz, R., Schoenfeld, H.-J., Broger, C., Loetscher, H. & Lesslauer, W. (1993). *Cell*, **73**, 431–445.
Battye, T. G. G., Kontogiannis, L., Johnson, O., Powell, H. R. & Leslie, A. G. W. (2011). *Acta Cryst.* D**67**, 271–281.
Brown, J., Esnouf, R. M., Jones, M. A., Linnell, J., Harlos, K., Hassan, A. B. & Jones, E. Y. (2002). *EMBO J.* **21**, 1054–1062.
Chen, V. B., Arendall, W. B., Headd, J. J., Keedy, D. A., Immormino, R. M., Kapral, G. J., Murray, L. W., Richardson, J. S. & Richardson, D. C. (2010). *Acta Cryst.* D**66**, 12–21.
Cianci, M., Helliwell, J. R. & Suzuki, A. (2008). *Acta Cryst.* D**64**, 1196–1209.
Cowtan, K. (1994). *Jnt CCP4/ESF–EACBM Newsl. Protein Crystallogr.* **31**, 34-38.
Dauter, Z., Dauter, M., de La Fortelle, E., Bricogne, G. & Sheldrick, G. M. (1999). *J. Mol. Biol.* **289**, 83–92.
Debreczeni, J. É., Bunkóczi, G., Girmann, B. & Sheldrick, G. M. (2003). *Acta Cryst.* D**59**, 393–395.
Debreczeni, J. É., Bunkóczi, G., Ma, Q., Blaser, H. & Sheldrick, G. M. (2003). *Acta Cryst.* D**59**, 688–696.
Emsley, P., Lohkamp, B., Scott, W. G. & Cowtan, K. (2010). *Acta Cryst.* D**66**, 486–501.
Evans, P. (2006). *Acta Cryst.* D**62**, 72–82.
Fischer, H., de Oliveira Neto, M., Napolitano, H. B., Polikarpov, I. & Craievich, A. F. (2010). *J. Appl. Cryst.* **43**, 101–109.

Gordon, E. J., Leonard, G. A., McSweeney, S. & Zagalsky, P. F. (2001). *Acta Cryst.* D**57**, 1230–1237.
Goulet, A., Vestergaard, G., Felisberto-Rodrigues, C., Campanacci, V., Garrett, R. A., Cambillau, C. & Ortiz-Lombardía, M. (2010). *Acta Cryst.* D**66**, 304–308.
Hendrickson, W. A. & Teeter, M. M. (1981). *Nature (London)*, **290**, 107–113.
Itoh, N. & Nagata, S. (1993). *J. Biol. Chem.* **268**, 10932–10937.
Kitago, Y., Watanabe, N. & Tanaka, I. (2005). *Acta Cryst.* D**61**, 1013–1021.
Klíma, M., Broučková, A., Koc, M. & Anděra, L. (2011). *Mol. Immunol.* **48**, 1439–1447.
Klíma, M., Zájedová, J., Doubravská, L. & Anděra, L. (2009). *Biochim. Biophys. Acta*, **1793**, 1579–1587.
Konarev, P. V., Volkov, V. V., Sokolova, A. V., Koch, M. H. J. & Svergun, D. I. (2003). *J. Appl. Cryst.* **36**, 1277–1282.
Körner, H. & Sedgwick, J. D. (1996). *Immunol. Cell Biol.* **74**, 465–472.
Kozin, M. B. & Svergun, D. I. (2001). *J. Appl. Cryst.* **34**, 33–41.
Kuester, M., Kemmerzehl, S., Dahms, S. O., Roeser, D. & Than, M. E. (2011). *J. Mol. Biol.* **409**, 189–201.
Lakomek, K., Dickmanns, A., Mueller, U., Kollmann, K., Deuschl, F., Berndt, A., Lübke, T. & Ficner, R. (2009). *Acta Cryst.* D**65**, 220–228.
Langer, G., Cohen, S. X., Lamzin, V. S. & Perrakis, A. (2008). *Nature Protoc.* **3**, 1171–1179.
Leslie, A. G. W. (2006). *Acta Cryst.* D**62**, 48–57.
Li, S. *et al.* (2002). *J. Biol. Chem.* **277**, 48596–48601.
Li, Y. *et al.* (2008). *Proteins*, **71**, 2109–2113.
Liu, Z.-J., Lin, D., Tempel, W., Praissman, J. L., Rose, J. P. & Wang, B.-C. (2005). *Acta Cryst.* D**61**, 520–527.
Liu, Z.-J., Vysotski, E. S., Chen, C.-J., Rose, J. P., Lee, J. & Wang, B.-C. (2000). *Protein Sci.* **9**, 2085–2093.
Madauss, K., Juzumiene, D., Waitt, G., Williams, J. & Williams, S. (2004). *Endocr. Res.* **30**, 775–785.
McCoy, A. J., Grosse-Kunstleve, R. W., Adams, P. D., Winn, M. D., Storoni, L. C. & Read, R. J. (2007). *J. Appl. Cryst.* **40**, 658–674.
Mi, S., Lee, X., Hu, Y., Ji, B., Shao, Z., Yang, W., Huang, G., Walus, L., Rhodes, K., Gong, B. J., Miller, R. H. & Pepinsky, R. B. (2011). *Nature Med.* **17**, 816–821.
Mukai, Y., Nakamura, T., Yoshikawa, M., Yoshioka, Y., Tsunoda, S., Nakagawa, S., Yamagata, Y. & Tsutsumi, Y. (2010). *Sci. Signal.* **3**, ra83.
Murshudov, G. N., Skubák, P., Lebedev, A. A., Pannu, N. S., Steiner, R. A., Nicholls, R. A., Winn, M. D., Long, F. & Vagin, A. A. (2011). *Acta Cryst.* D**67**, 355–367.
Nagata, S. & Golstein, P. (1995). *Science*, **267**, 1449–1456.
Nagem, R. A. P., Ambrosio, A. L. B., Rojas, A. L., Navarro, M. V. A. S., Golubev, A. M., Garratt, R. C. & Polikarpov, I. (2005). *Acta Cryst.* D**61**, 1022–1030.
Naismith, J. H., Devine, T. Q., Brandhuber, B. J. & Sprang, S. R. (1995). *J. Biol. Chem.* **270**, 13303–13307.
Naismith, J. H., Devine, T. Q., Kohno, T. & Sprang, S. R. (1996). *Structure*, **4**, 1251–1262.
Naismith, J. H. & Sprang, S. R. (1998). *Trends Biochem. Sci.* **23**, 74–79.
Nan, J., Zhou, Y., Yang, C., Brostromer, E., Kristensen, O. & Su, X.-D. (2009). *Acta Cryst.* D**65**, 440–448.
Nikolaev, A., McLaughlin, T., O'Leary, D. D. & Tessier-Lavigne, M. (2009). *Nature (London)*, **457**, 981–989.
Otwinowski, Z. & Minor, W. (1997). *Methods Enzymol.* **276**, 307–326.
Pannu, N. S., Murshudov, G. N., Dodson, E. J. & Read, R. J. (1998). *Acta Cryst.* D**54**, 1285–1294.
Ramagopal, U. A., Dauter, M. & Dauter, Z. (2003). *Acta Cryst.* D**59**, 1020–1027.
Ren, H., Wang, L., Bennett, M., Liang, Y., Zheng, X., Lu, F., Li, L., Nan, J., Luo, M., Eriksson, S., Zhang, C. & Su, X.-D. (2005). *Proc. Natl Acad. Sci. USA*, **102**, 303–308.
Sarma, G. N. & Karplus, P. A. (2006). *Acta Cryst.* D**62**, 707–716.
Sheldrick, G. M. (2008). *Acta Cryst.* A**64**, 112–122.
Su, J., Li, Y., Shaw, N., Zhou, W., Zhang, M., Xu, H., Wang, B.-C. & Liu, Z.-J. (2010). *Protein Cell*, **1**, 453–458.
Svergun, D. I. (1992). *J. Appl. Cryst.* **25**, 495–503.
Svergun, D. I., Petoukhov, M. V. & Koch, M. H. (2001). *Biophys. J.* **80**, 2946–2953.
Tartaglia, L. A., Ayres, T. M., Wong, G. H. W. & Goeddel, D. V. (1993). *Cell*, **74**, 845–853.
Volkov, V. V. & Svergun, D. I. (2003). *J. Appl. Cryst.* **36**, 860–864.
Wagner, A., Pieren, M., Schulze-Briese, C., Ballmer-Hofer, K. & Prota, A. E. (2006). *Acta Cryst.* D**62**, 1430–1434.
Wang, B.-C. (1985). *Methods Enzymol.* **115**, 90–112.
Watanabe, N., Kitago, Y., Tanaka, I., Wang, J., Gu, Y., Zheng, C. & Fan, H. (2005). *Acta Cryst.* D**61**, 1533–1540.
Weiss, M. S., Mander, G., Hedderich, R., Diederichs, K., Ermler, U. & Warkentin, E. (2004). *Acta Cryst.* D**60**, 686–695.
Weiss, M. S., Sicker, T., Djinovic-Carugo, K. & Hilgenfeld, R. (2001). *Acta Cryst.* D**57**, 689–695.
Wilson, N. S., Dixit, V. & Ashkenazi, A. (2009). *Nature Immunol.* **10**, 348–355.
Winn, M. D. *et al.* (2011). *Acta Cryst.* D**67**, 235–242.
Yang, C. & Pflugrath, J. W. (2001). *Acta Cryst.* D**57**, 1480–1490.
Yang, C., Pflugrath, J. W., Courville, D. A., Stence, C. N. & Ferrara, J. D. (2003). *Acta Cryst.* D**59**, 1943–1957.